



Contents lists available at ScienceDirect

Journal of the Taiwan Institute of Chemical Engineers

journal homepage: www.elsevier.com/locate/jtice

Facile synthesis of sulfated mesoporous Zr/ZSM-5 with improved Brønsted acidity and superior activity over SZr/Ag, SZr/Ti, and SZr/W in transforming UFO into biodiesel

Yahaya Muhammad Sani^{a,b}, Peter Adeniyi Alaba^a, Aisha Olatope Raji-Yahya^b, A.R. Abdul Aziz^{a,*}, Wan Mohd Ashri Wan Daud^a

^a Department of Chemical Engineering, University of Malaya, 50603 Kuala Lumpur, Malaysia

^b Department of Chemical Engineering, Ahmadu Bello University, 870001 Zaria, Nigeria

ARTICLE INFO

Article history:

Received 11 April 2015

Revised 9 September 2015

Accepted 6 October 2015

Available online xxx

Keywords:

Zirconia

Zeolite

Solid acid catalyst

High free fatty acid

Biodiesel

ABSTRACT

On the basis of the interplay between the metal function of oxo-anions, and structure of zeolites and its acidic properties, we report an innovative approach for enhancing acidity of sulfated zirconia, SZ. This concerns the superiority of SZ comprised of single-Brønsted acid sites dispersed on ZSM-5 over Ag, Ti and W. The influence of doping ZrO₂ on MFI framework of ZSM-5 was studied against other composite catalysts characterized by temperature-programmed desorption of ammonia (NH₃-TPD), IR spectra of pyridine adsorption, N₂ sorption, powder X-ray diffraction, elemental analysis via FE-SEM and EDX. Results showed uniform pore size, high mesopore volume, high surface area, and acid densities on the catalysts. Despite lower pore size distribution, Zr/ZSM-5 exhibited highest total acidity (0.75 mmol/g), and activity in converting >95% used frying oil (48 wt.%) over SZr/Ag, SZr/Ti, and SZr/W. This is outstanding considering the lower reaction parameter of 5 h, 5:1 methanol-to-oil ratio, and 200 °C compared to prior arts. Evidently, structure and strength of Brønsted acids have direct effect on the catalytic activity of the materials. This study also illustrated prospects of converting wastes into biodiesel, which is important especially against the backdrop of the current plummeting price of Brent crude oil.

© 2015 Taiwan Institute of Chemical Engineers. Published by Elsevier B.V. All rights reserved.

1. Introduction

As the price of Brent oil plummeted below USD45/barrel in the third quarter of 2015, the prominence, and sustenance of biofuels in general, and biodiesel in particular, faces greater challenges. The heavily footed subsidy that fossil fuels enjoy from governmental agencies exacerbates this problem further. Consequently, for biodiesel to maintain its indomitability as sustainable energy alternative beyond the 21st century, urgent and concerted efforts must be initiated from reactor engineering and catalysis [1,2]. From materials chemistry perspective, many studies have investigated the performances of a wide range of bifunctional solid acids catalysts such as WO₃/ZrO₂ [3], WO₃/SnO₂ [4], Mo-Mn/Al₂O₃-15 wt.% MgO [5], WO₃/ZrO₂ [6,7] and SO₄²⁻/TiO [8] designed to incorporate synergistic effect in catalysis. However, despite the capability of converting

different feedstock oils to fatty acid methyl esters, FAME there is need for improvements.

For instance, WO₃/SnO₂ required 43 methanol-to-oil ratio to achieve a 78% yield [4], WO₃/ZrO₂ gave ~100% conversion after 20 h at 200 °C [6] and 70% conversion from used frying oil, UFO [7]. Similarly, the difficulty in synthesis and high production cost of SO₄²⁻/TiO₂ hinder its industrial application [8]. WO₃/ZrO₂ converted more than 90% soybean oil during transesterification at 250 °C [6] while SO₄²⁻/TiO₂, SO₄²⁻/ZrO₂, and WO₃/ZrO₂ converted 100, 99, and 94% *n*-octanoic acid respectively during esterification at 175 °C. In addition, longer reaction time (2047 min) was necessary for obtaining 50% conversion with tungstated zirconia with the acid site densities exhibiting ca. 95% of the original values. The long duration promoted adsorption of intermediates and products with subsequent deactivation.

Conversely, some results obtained from transesterification with zeolites were not as encouraging. For instance, despite high alcohol-to-oil molar ratio (14.5:1), Shu et al. [9] reported only 48.9 wt.% FAME conversion after 4 h with zeolite beta modified with La³⁺. Equally, Mordenite (HMOR) and H⁺ ion exchanged ZSM-5 (HMF1) zeolites [10] converted 80% of oleic acid with >0.06 mmol/g acid amount

* Corresponding author Tel.: +60 3 7967 5300; fax: +60 3 79675319.

E-mail addresses: ymsani@siswa.um.edu.my (Y.M. Sani), adeniyipee@live.com (P.A. Alaba), raji.aisha@gmail.com (A.O. Raji-Yahya), azizraman@um.edu.my, raja.shazrin@gmail.com (A.R. Abdul Aziz), ashri@um.edu.my (W.M.A.W. Daud).

<http://dx.doi.org/10.1016/j.jtice.2015.10.010>

1876-1070/© 2015 Taiwan Institute of Chemical Engineers. Published by Elsevier B.V. All rights reserved.

to biodiesel. High reaction temperature of 500 °C was necessary to achieve ca. 100% conversion over H-ZSM-5 [$S_{\text{BET}} = 377 \text{ m}^2/\text{g}$, acidity density = 382 $\mu\text{mol}/\text{gcat}$] after 20 min [11]. Consequently, Kiss et al. [12] posited that lower catalytic activity of zeolites is due to the small pores, which limits diffusion of large fatty acid molecules. However, Dasari et al. [13] obtained 95% conversion without catalyst, albeit at high pressures of 45–65 MPa and high temperatures of 350–500 °C. Nonetheless, Sasidharan and Kumar [14] were able to obtain 85% and 80% conversion from beta-keto esters with solid acid La-Beta and H-Y zeolites respectively. Evidently, the nature of the oil employed by Sasidharan and Kumar [14] also contributed to the encouraging results. Moreover, the high-silica in Zeolite Socony Mobil-5, ZSM-5 [Mordenite framework inverted (MFI) type and a member of the pentasil family] gives it special properties. Depending on the Si/Al ratio, ZSM-5 is moderately hydrophilic to highly hydrophobic unlike types A, X and Y zeolites, which are very hydrophilic. Another important factor that ensures this desirable property is the type and number of cations compensating the lattice charge. Further, the hydrogen form is obtainable without losing significant Al directly via zeolite exchange in dilute acid because of its acid (down to pH 3) and temperature (> 1000 °C) stability.

Further, the acidity of crystalline aluminosilicate zeolites may be fine-tuned by appropriate manipulation of $\text{SiO}_2/\text{Al}_2\text{O}_3$ molar ratio. Such manipulations have significant effect on the activity (i.e. the hydrophobicity and acidity of the zeolite), performance, and its affinity for water. Interestingly, the structure of ZSM-5 also allows the introduction of alternative T-atoms such B, Be, Al, Si, Ga, Fe, Ge, etc. during synthesis [15]. The nature of positive simple counterions from these T-atoms also determines the acidic catalytic power of the zeolite. Thus, its catalytic properties are amenable to adjustments for the desired catalytic process, which include interchanging other elements within the framework constituents, or by modifying the zeolitic material. These intriguing attributes of ZSM-5 explain its acceptability as efficient catalytic material with wide range of applications in the laboratory as well as the industry. However, these advantages do come with attendant problems. These include deactivation and a drop in conversion from reaction of organic species catalyzed by zeolite with lower Si/Al ratio, which causes higher affinity toward water.

However, despite the numerous encouraging results highlighted above, attendant viscosity and poor miscibility of light alcohols with low-grade oil feedstocks hampers the use of new heterogeneous catalysts. This explains why to date, the wide range of commercially available polymeric and inorganic solid acids have lower activity when compared with their base-catalyzed routes [16]. This necessitates the application of higher reaction temperatures to achieve appreciable conversions. Other limitations include rapid on-stream deactivation because of impurities in high concentrations, such as moisture, acid, and heavy metals. Aside this arduous challenge, another contending issue is regional availability, which determines the quest and cost for utilizing non-edible, low-grade oil sources. Notwithstanding their comparable lower activity, solid acids are less susceptible to FFA contaminants common with unrefined feedstocks than their solid base equivalents [16]. Moreover, they are able to esterify free fatty acids, FFA into esters, and transesterify triglycerides, TG into FAME simultaneously without pretreatment, and saponification; thus minimizing the processing steps in biodiesel production [17–19]. Intriguingly, zirconium is active at lower temperatures than zeolite catalysts, while zeolites are generally more acidic than zirconia. Notwithstanding this and the extensive research on the factors affecting the acidity of sulfated zirconia, SZr there is no information in open literature that concerns biodiesel production with mesoporous SZr dispersed over ZSM-5. Consequently, the present contribution aims to demonstrate the superiority of mesoporous sulfated zirconia comprised of Brønsted acid sites dispersed on ZSM-5 over Ag, Ti and W supports. To achieve this, the present study investigated an

innovative approach of enhancing acidity of sulfated, robust bifunctional composite catalysts that could withstand unfavorable constituents highlighted above. This was premised on the basis of the interplay between metal function of modified oxo-anions and pore structure of zeolites and its strong acidic properties.

2. Materials and method

2.1. Catalyst preparation

The following describes the easy, and undemanding catalyst preparation employed for this study. Sigma-Aldrich, Germany supplied all chemical reagents. To ensure reproducibility, all sample preparations were carried out in replicates. A required amount of ammonium hydroxide solution precipitated the active constituents from zirconium oxynitrate hydrate (99%) at pH of 10 under vigorous stirring. Subsequently, the filtrate was washed with de-ionized water to minimize the nitrate ion concentration. For comparison and optimization, about 2.5 to 25% each of AgNO_3 ($\geq 99.0\%$), titanium nitride (TiN; $< 3 \mu\text{m}$), ammonium metatungstate hydrate, $(\text{NH}_4)_6\text{H}_2\text{W}_{12}\text{O}_{40}\cdot x\text{H}_2\text{O}$ (99.99% trace metals basis), and ZSM-5 (Si/Al = 20.01) were separately soaked in the precipitated zirconium solution at ambient conditions for 4 h. The solution contained exact amount of liquid which filled the pore volume of the support. This facilitated good contact (impregnation) between the metal precursors and the porous support. The supernatant was decanted after proper saturation and infusion of the metal elements. Thereafter, sufficient (not in excess) 0.5-M H_2SO_4 was added to the impregnated mixed oxides, and kept at room temperature to ensure the incorporation of appropriate doubly charged sulfate oxo-anions. After drying in an oven at 120 °C for 24 h, the samples were calcined separately at 550 °C for 4 h. This process was optimized and catalytic materials were designated SZr/Ag, SZr/Ti, SZr/W, and SZr/ZSM-5. The following discussion would mainly be regarding these four samples, and in some instances, in comparison with the ZSM-5.

2.2. Catalyst characterization

Field emission scanning electron microscopy (FE-SEM) FEI QUANTA™ 450 FEG type 2033/14 (Czech Republic) unit with 30 kV accelerating voltage analyzed the surface morphology and topology. An energy dispersive X-ray spectrometer (EDX) from the same unit revealed the surface elemental composition variation of the catalysts. The samples were evenly distributed on a double sided, black carbon tape glued on an aluminum stub and put under vacuum for 10 min prior to the analysis. Similarly, powder XRD and BET analyses elucidated the structural and textural properties of the catalysts respectively. Phillips X'pert diffractometer (The Netherlands) with $\text{CuK}\alpha$ radiation ($\lambda = 1.54056 \text{ \AA}$) at a scanning speed of $0.05^\circ \text{ s}^{-1}$ within 2θ range of 5° to 70° at 40 mA and 40 kV analyzed the XRD patterns, the crystal phase and structure of the samples. A Micromeritics TriStar II (USA) with accelerated surface area porosity (ASAP) 3020 at $-196.15 \text{ }^\circ\text{C}$ in liquid nitrogen, determined the specific surface area, pore size and the pore volume of the catalytic materials. Degassing the catalysts at 120 °C for 3 h under a vacuum eliminated any physisorbed volatiles and impurities. These were kept in liquid nitrogen temperature for nitrogen adsorption.

An AutoChem 2920 (Micromeritics) evaluated the acid density profiles via ammonia temperature-programmed desorption (NH_3 -TPD). Calibrating the equipment with 10% NH_3 in He before the analysis guarantees ascertaining the exact amount of gas consumed during the experiment. For each analysis, He flow (20 mL/min) for 1 h at 700 °C degasses about 0.10 g of the synthesized material housed in a quartz U-tube. After cooling to 80 °C, 10% NH_3 in He flowing at 20 mL/min for 40 min saturates the sample. A steady temperature ramp of 120 °C ensured proper NH_3 adsorption. Changing the gas

flow to He at 20 mL/min for 30 min over the catalyst removed the physisorbed NH_3 . Elevating the temperature ramp from 80 °C to 700 °C at 10 °C/min under flowing He at 20 mL/min after the baseline stabilizes produces distinct TPD profile. Similarly, the TCD detector revealed the amount of NH_3 consumed, which determines the Brønsted and Lewis acid sites in the catalyst. IR spectra of adsorbed pyridine were taken on a Bruker Fourier transform infrared (FT-IR) Tensor 27 spectrometer (Germany). The apparatus has a spectral range of 7500 to 370 cm^{-1} with more than 1 cm^{-1} apodized resolution and a standard ATR beam splitter. The samples were outgassed at 300 °C for 4 h under vacuum, and cooled to room temperature. Pyridine was then admitted into the samples and the IR spectra of adsorbed pyridine were recorded at room temperature.

2.3. Production of fatty acid methyl esters

Heating the catalysts at 200 °C for 1 h before the reaction ensured activation by evacuating any adsorbed water and other volatiles. Thereafter, the catalytic activity of the catalysts in simultaneous esterification and transesterification of UFO (FFA = 48 wt.%) with methanol was determined in a 100 mL autoclave stainless-steel reactor supplied by AmAr Equipment Pvt., Ltd. (Mumbai). Constant stirring at 550 rpm ensured good contact between the catalyst and the reaction mixture. A water bath attached to the autoclave maintained the reaction temperature in the range of 190–200 °C during the reaction. Preliminary optimization showed that a 5:1 methanol-to-oil molar ratio and 2 wt.% catalyst loading were optimal for the reaction. At the end of the 5 h reaction time, it took more than 6 h for the product [ester or oil phase (biodiesel) and the upper aqueous phase (glycerol)] to settle into two distinct layers because of the initial translucent nature of biodiesel. The two distinct phases were separated by simple decanting. Centrifugation, water washing, and drying with anhydrous sodium sulfate facilitated the recovery of the FAME by purifying it from excess methanol and other impurities such as residual catalyst.

3. Results and discussion

The following discussion concerns the various characterizations such as NH_3 -TPD, IR spectroscopy, and structural analyses performed on the catalysts to ascertain which properties have significant influence in converting the UFO into FAMES.

3.1. Results of catalyst characterization

3.1.1. Acid density measurement via NH_3 -TPD

Temperature-programmed ammonia desorption, NH_3 -TPD revealed information regarding the distribution and type of acid sites on the catalysts (Table 1). Fig. 1(a) and (b) shows representative NH_3 -TPD profiles of the parent ZSM-5, and SZr/W, SZr/Ag, and SZr/Ti modified catalysts calcined at 550 °C for 4 h. We classified the acid sites corresponding to base desorption at 100–240 °C, 240–340 °C, and 340–500 °C as weak, intermediate, and strong acid sites, respectively. The peak pattern of modified SZr/ZSM-5 reveals similar profile as the parent ZSM-5. Expectedly, the parent ZSM-5 contained 5-fold more acid number than the composite SZr/ZSM-5, and even more than the other mixed oxides. The probable explanation for the significant decrease in the acidity of the SZr/ZSM-5 compared with ZSM-5 is the combined effect of the hydroxyl Al(OH)Si bridging groups with ZrO_2 species [20]. However, SZr/ZSM-5 exhibited higher acidity than the other materials because of its available protons for donation. Notably, SZr/W generated strong Brønsted and Lewis acidity because of the extensive polymerization of W species from its sulfate groups. This explains the difference between SZr/W and SZr/Ag, SZr/Ti. However, SZr/W, SZr/Ag, and SZr/Ti have comparable acidity. Except for SZr/Ti

(flat and broad), the NH_3 -TPD curves revealed sharp NH_3 desorption peaks. This indicated the presence of broad acid sites distribution on the synthesized catalysts. The shapes of the NH_3 -TPD profiles were consistent with those reported for comparable mesoporous zirconium titanium oxide nanospheres [21–24].

The source compounds that supply aluminum during the synthesis of zeolites determine the acidity of mesoporous zeolites. Similarly, zeolite type, Si/Al ratio, and metal loading have significant effect on both total acidity (mmol/g) and the acid strength distribution of the catalyst. This explains the high acidity (3.71 mmol/g) of the source ZSM-5 employed in the present study. Incidentally, Čejka et al. [25] reported higher acidity of 4.99 mmol/g for H-ZSM-5 (Si/Al ratio = 36; average crystal size = 6 μm). Further, Song et al. [26] obtained similar total acidity (2.42, 1.53, 2.90, and 3.12 mmol/g) from [sodium aluminate (Si/Al ratio = 49), H-mordenite (Si/Al ratio = 21.0), HY-2 (Si/Al ratio = 5.0), and HY-2 (Si/Al ratio = 5.0)] respectively. Markedly, all synthesized materials, except SZr/Ag and SZr/W, predominantly exhibited the weak Lewis acid property. This is because Brønsted sites get desorbed at temperatures higher than 400 °C. Zou and Lin [24] and Das et al. [27] assigned broad peaks at temperatures below 600 °C to a conglomerate of overlapping component peaks. These peaks may include ammonia desorption from bound strong Lewis acid sites, NH_4^+ ions decomposition and those released from weak Lewis acid sites. The latter desorption may also include coordinately unsaturated titanium and zirconium ions. The low-temperature peak desorption of bulk titanium oxide are representative of the weak support interaction, which corroborated a report by Mile et al. [28].

A notable increase in the number of acid sites was observed in the mixed oxide catalysts compared to single oxide SZr. This observation is in complete accordance with a previous report [29] that mixed oxides generate more acid sites than single oxides. This is premised on one of two mechanisms: (a) zirconium atoms substituting some of the oxide atoms or (b) large dispersion effect on the surface of the mixed oxide by the ZrO_2 or the other oxide. The strength of the acid site density was in the following order: ZSM-5 > SZr/ZSM-5 \gg SZr/Ag > SZr/Ti > SZr/W. This sequence highlights the natural acidity of ZSM-5 in comparison to the generated Brønsted acid sites on the other mixed oxides introduced by sulfate anions on the surface of the catalysts. The discussion in the results section further illustrated the effect of acid density on the activity of the simultaneous esterification of FFA and transesterification of TG. Mostly, infrared adsorption experiments with basic probe molecules such as ammonia, pyridine, and acetonitrile differentiate Brønsted or Lewis acid sites.

However, the measurement conditions employed such as desorption temperature, determine the results of the analysis. Further, the adsorption of ammonia is not specific to Brønsted sites. These highlight the possibility of non Brønsted sites adsorbing more, and hence exhibiting stronger acidity than Brønsted sites. Hence, TPD results are helpful, but with careful interpretation of data. Evidently, no single method can give all the details of the acidity of solid acid catalyst. For example, Jacobs and Von Ballmoos [30] distinguished the Brønsted sites in H-ZSM-5 by a well-defined stretching frequency, 3605 cm^{-1} while Ward [31] and Angell and Schaffer [32] distinguished those in H-Y by 3640 and 3540 cm^{-1} stretching. Nonetheless, it is difficult to quantify the concentrations of these sites because of the overlapping features in the spectra. Evaluating the concentration of the protonated bases in the solid is one way of circumventing this challenge. The characterization of pyridine adsorption by infrared spectroscopy is one most popular application of this technique [33]. Therefore, this study employed NH_3 -TPD and IR-Spectroscopy of chemisorbed pyridine to get accurate picture about the acidity of the synthesized catalysts.

3.1.2. Acid density probed by IR-spectroscopy of chemisorbed pyridine

Pyridine adsorption measured by IR spectroscopy revealed the strength and types of acid sites of catalysts. The formation of

Table 1
Textural properties and acidity of synthesized sulfated zirconia revealed by BET and NH₃-TPD methods respectively.

Sample ID	Surface area (m ² /g)	Pore vol. (cm ³ /g)	Pore size (nm)	Acidity (mmol/g)
ZSM-5	385.20	0.15	3.04	3.71
SZr/ZSM-5	107.25	0.12	5.10	0.75
SZr/Ag	15.97	0.08	20.11	0.14
SZr/Ti	12.90	0.05	14.53	0.09
SZr/W	72.13	0.10	5.37	0.05

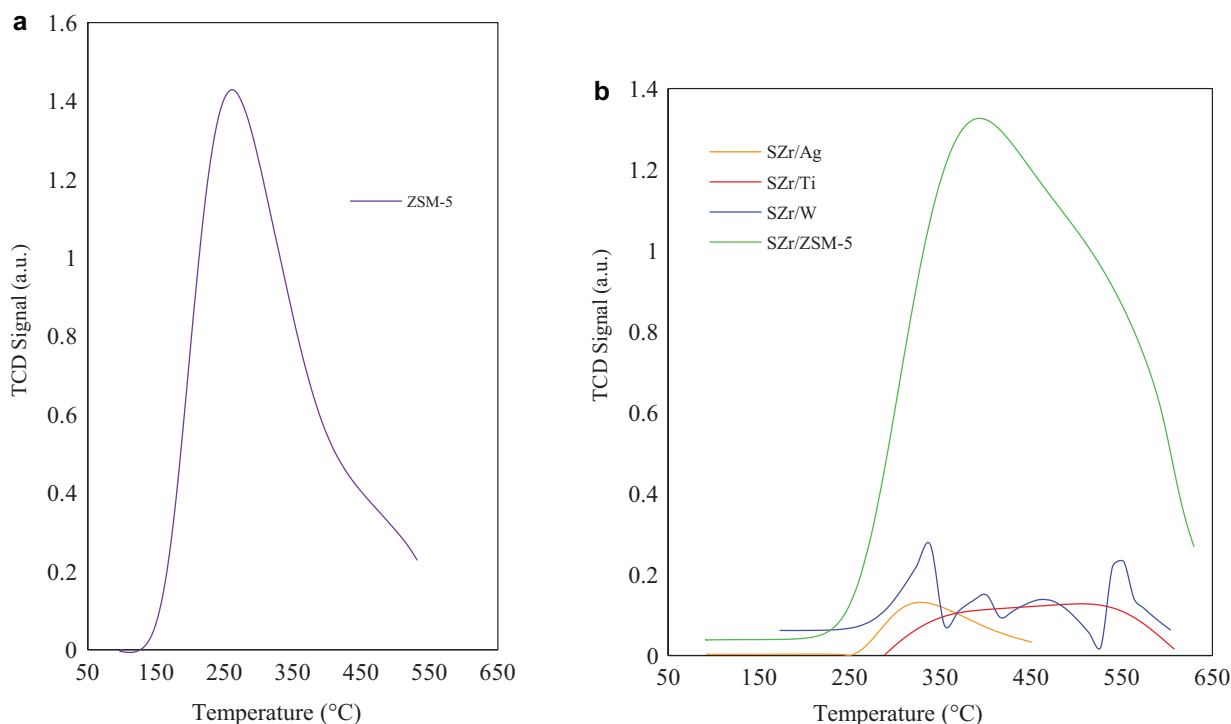


Fig. 1. (a) NH₃-temperature-programmed desorption profiles for the parent ZSM-5 and (b) synthesized SZr/Ag, SZr/Ti, SZr/W, and SZr/ZSM-5 catalysts.

stoichiometric adsorption complex on the acid sites by pyridine makes this acid measurement distinctive. Pyridine accepts proton to form pyridinium ion on the Brønsted sites whereas an adduct forms at the Lewis sites by donating lone pair of electrons. Partial hydrolysis of some framework aluminum atoms occurs after steam treatment at 300 °C to form non-tetrahedral symmetric aluminum atoms. These act as strong electron withdrawal centers for the remaining tetrahedral framework aluminum atoms that facilitate the formation of stronger Brønsted acids. Further, the technique exploits the modification in chemical nature of the adsorbed species. Moreover, the pyridine adsorbed on Brønsted sites and Lewis sites have different wavenumbers because of difference in bonding nature. The ring stretching vibration at *ca.* 1540 (1515–1565 cm⁻¹) and 1450 cm⁻¹ (1435–1470 cm⁻¹) to protonated pyridine, *i.e.* pyridinium cation (Brønsted acid sites) and coordinated pyridine (Lewis acid sites) appear, respectively. Fig. 2 presents the acidity distribution (variation of IR bands in 1400–1700 cm⁻¹ region) of ZSM-5, SZr/ZSM-5, SZr/Ag, SZr/Ti, and SZr/W.

Expectedly, the parent ZSM-5 exhibited stronger sites of both Brønsted and Lewis acids than the remaining four samples. The profiles of synthesized catalytic materials reveal similar patterns as the parent sample. The trend of the Brønsted acid site strength was similar to the one obtained by NH₃-TPD in the following order: ZSM-5 > SZr/ZSM-5 > SZr/Ti > SZr/Ag > SZr/W. However, the trend was different for the Lewis acid site strength in the following order: ZSM-5 > SZr/ZSM-5 > SZr/Ag > SZr/Ti > SZr/W. The three prominent bands

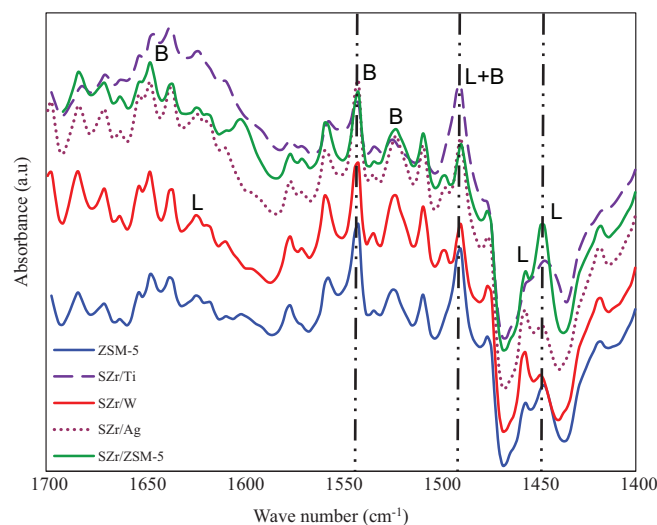


Fig. 2. Room-temperature infrared spectra of adsorbed pyridine on ZSM-5, SZr/ZSM-5, SZr/Ag, SZr/Ti, and SZr/W after outgassing at 300 °C for 4 h.

in the 1425–1575 region are representative of: (a) the C–C stretch at ~1450 cm⁻¹ arising from a coordinatively bonded pyridine complex that designates the presence of Lewis sites. (b) The C–C stretching

vibration of the pyridinium ion at $\sim 1540\text{ cm}^{-1}$ that is typically used for identifying Brønsted sites. (c) The peak at $\sim 1490\text{ cm}^{-1}$ arising from the interaction of pyridine species with both Brønsted and Lewis acid sites. All the samples exhibited the IR bands due to hydrogen-bonded pyridine at 1447 cm^{-1} , but only the parent ZSM-5 and modified SZr/ZSM-5 showed peaks at 1599 cm^{-1} . This is because of the difference in the Si/Al ratios of the samples. Similarly, the peaks at 1455 and 1623 cm^{-1} exhibited by all the samples indicate pyridine adsorbed on Lewis acid sites, while those at 1533 and 1647 cm^{-1} highlight pyridine adsorbed on Brønsted acid sites. Pyridine associated with both Lewis and Brønsted acid sites appear at 1490 cm^{-1} . Previously, Jin and Li [34] and Emeis [35] reported similar analysis on the distribution of acid sites.

Evidently, the acidity of the materials determined by NH_3 -TPD supersedes that of their counterparts determined by the pyridine adsorbed IR method. This is plausibly because of the differences in the molecular size of the basic probe molecules. Ammonia molecule penetrates through more pores because of its smaller molecules than the larger molecules of pyridine [36]. Table 2 presents a summary of the frequencies and reported extinction coefficients assigned to adsorbed species on acid sites.

3.1.3. Powder X-ray diffraction analysis

The highly crystalline characteristic peaks at 2θ value of 7.87 , 8.81 , 23.09 , 23.86 , 24.34 , 29.20 and 29.88 confirmed ZSM-5 support according to the JCPDS Card No. 00-044-0002 [38]. The powder X-ray pattern peaks of the ZSM-5 showed typical MFI topology, whereas the modified SZr/ZSM-5 patterns indicated retained ZrO_2 crystallinity and novel crystalline phases (Fig. 3). The loss of intense ZSM-5 peaks was due to the effects of acid treatment, ZrO_2 and ZSM-5 inter-particle interaction and calcination during the synthesis stage as earlier noted. This indicates that ZrO_2 species were not merely dispersed on the zeolite, but might have replaced some of the alternative T-atoms. This interaction resulted in the almost disappearance of peaks with high intensities around $2\theta = 7^\circ$, 8° , 23° and 24° , and emergence of typical zirconium peaks at 28° , 30° , 50° and 60° . This further confirmed that ZrO_2 particles were not merely dispersed, but rather caused changes in the lattice structure of the zeolite.

The XRD diffractograms of all the samples revealed a tetragonal-monoclinic phase transition. The XRD patterns also showed the significant impact of calcination temperature and precursor concentration on the crystal phase and crystallite size. The formation of the monoclinic phase (peaks at $2\theta = 28.21^\circ$ and $2\theta = 31.51^\circ$) because of the increase of the crystallite size as function of temperature lowers the content of tetragonal phase ($2\theta = 30^\circ$). This is in agreement with the Garvie Theory [39]. Further, except for SZr/Ti, it is evident that characteristic tetragonal peak at $2\theta = 30^\circ$ was more prominent than those of the monoclinic phases were. However, the remaining monoclinic peaks were more prominent than the reduced tetragonal phases. In addition, the intensity of the peaks reflected both adsorption and the amount of phase in the synthesized materials. For instance, the monoclinic phase present on the parent TiN at $2\theta = 37^\circ$, 43° , 62° , 75° and 79° disappeared after the modification with zirconia. These were replaced with tetragonal phase typical of zirconia at 24° , 28° , 34° , and 50° . Furthermore, broad nature of the peaks indicates the nanocrystalline nature of the materials. Also, the lower surface energy of the tetragonal phase when compared to monoclinic phase ensured transformation of the metastable tetragonal phase [40].

3.1.4. Measurement of physicochemical properties

The measurement of the specific surface area, S_{BET} was according to the BET method from the nitrogen adsorption isotherms obtained at -196.15°C . Table 1 presents the textural properties and acidity of the mesoporous mixed oxide catalysts. Fig. 3(a) presents the nitrogen sorption isotherms of all the samples. The parent ZSM-5 sample exhibited a characteristic monolayer formation at lower relative

pressure followed by few molecular layers typical of Type I isotherm. This is because at higher pressures, adsorbate fills the micropores and restricts additional adsorption as represented by the plateau on Fig. 4(a). However, the BET surface area for all synthesized samples decreased significantly after modification with ZrO_2 compared to the parent ZSM-5. Equally, the pore size, which facilitates diffusion benefits, was in the following order: $\text{SZr/Ag} > \text{SZr/Ti} > \text{SZr/W} > \text{SZr/ZSM-5} > \text{ZSM-5}$. All the synthesized catalysts revealed mesoporous ($2 < d_p < 50\text{ nm}$) structures that permits the TG molecule (which requires a critical diameter of 2 to 4 nm) access to the active sites within the materials (Table 1, Fig. 3) [2]. The difference in chemical composition of the catalytic materials plausibly explains the significant variations in textural and catalytic activities (Fig. 4a and b). Thus, for instance, SZr/ZSM-5 exhibited lower pore size (5.10 nm) than those of the other mixed oxide catalysts. These results suggest that the channels of SZr/ZSM-5 could get occluded easily and may result in mass transfer limitation. This is because a TG molecule requires a critical diameter or the smallest access cylinder of 2 to 4 nm [12,41].

The adsorption isotherm of all samples with exception of ZSM-5, followed type-IV IUPAC classification for mesoporous materials with capillary condensation taking place at higher pressures of adsorbate depicting a hysteresis loop [42]. The steep N_2 -uptake emphasized crystalline agglomeration of the plate-like, nano-sized particles containing slit-shaped pores. This resulted from inter-particle interaction and voids formed by the agglomeration which are typical of H_2 hysteresis during the catalyst synthesis. This observation is in accordance to the IUPAC classification, which is generally observed for mesoporous solids, thereby confirming the enhanced textural properties of SZr/ZSM-5 as seen in Table 1. Conversely, the low P/P_0 region for ZSM-5 revealed distinct increase in adsorbate volume with a tight hysteresis loop in the high P/P_0 region. This highlighted the occurrence of micropores evident from Fig. 3(b). Provided the effect of thermal or acid treatments were not excessive to destroy the aluminosilicate structural template, amorphization *via* morphological variation of erstwhile crystalline material, usually facilitates textural property enhancement [43]. However, the pattern of parent ZSM-5 was apparently destroyed after the modification that produced SZr/ZSM-5. Consequently, we attributed the superior properties observed on SZr/ZSM-5 from Table 1, BET results (Fig. 4) and SEM analysis (Figs 5–7) in comparison to other materials on the acidity of SZr/ZSM-5. This is because despite the destruction of crystallographic phase of ZSM-5 from SZr/ZSM-5, the process stabilized the mesostructure channels, and ensured higher catalytic performance on SZr/ZSM-5 than that of SZr/Ti, SZr/Ag, and SZr/W synthesized under similar conditions. These outcomes bring to light the effect that hydrogen H^+ has on Brønsted acidity and their influence on their ability to catalyze the transesterification reaction. The compared acidities of the other catalysts evidenced the observation regarding the acidic catalytic power of the zeolite influenced by nature of the cations.

3.1.5. Scanning electron microscopy

Scanning electron micrographs, SEM (Figs. 5–12) illustrates the surface microstructure of all the catalysts and the morphology of parent ZSM-5 as studied *via* FE-SEM. The FE-SEM micrographs (Figs. 4a–6b) revealed a change in the morphology of parent ZSM-5 and zirconia upon modification with species of both components and sulfate ions. Similarly, the variation in elemental compositions is vividly noticeable from the EDX graphs. The morphology of ZSM-5 suggested agglomerates of micro-sized hexagonal crystal prisms. However, ZrO_2 incorporation, acid treatment and calcination, caused large degree of morphological variation in the SZr/ZSM-5 (Fig. 7) as highlighted above.

The different constituents were homogeneously processed into solid particles of uneven dimensions. The EDX analysis of the surface elemental composition (Fig. 8b) revealed the presence of zirconium (87.17 wt.%), silica (9.72 wt.%), aluminum (1.49 wt.%) and sulfur

Table 2

Wave number frequencies and extinction coefficients of IR absorption spectra designated to typical probe molecules adsorbed on acid sites [35,37].

		Brønsted	Lewis
Ammonia	Frequency (cm ⁻¹)	1460	1620
	IR mode	$\delta(\text{NH}_4^+)_{\text{asym.}}$	$\delta(\text{NH}_3)_{\text{asym.}}$
	Extinction coefficient (ϵ)	14.7 m ² /mol	2.2 m ² /mol
Pyridine (C ₅ H ₅ N)	Frequency (cm ⁻¹)	1540	1450
	IR mode	Ring stretch (PyH ⁺)	Ring stretch (Py)
	Extinction coefficient (ϵ)	0.72 m ² /mol	2.23 m ² /mol
D ₃ -cetonitrile (CD ₃ CN)	Frequency (cm ⁻¹)	2297	2325, 2310
	IR mode	$\nu(\text{C}\equiv\text{N})\text{-B}$	$\nu(\text{C}\equiv\text{N})\text{-L}_{\text{strong, weak}}$
	Extinction coefficient (ϵ)	2.05 cm/ μmol	3.60 cm/ μmol

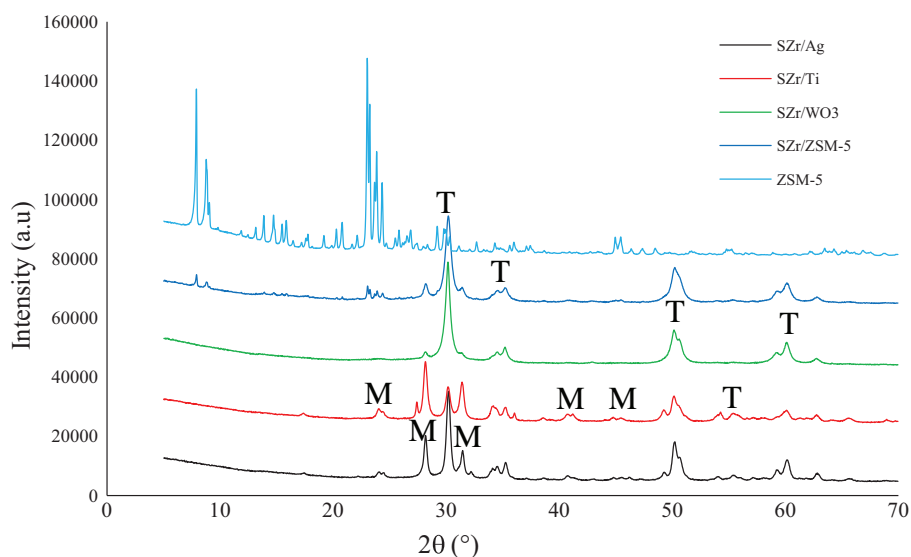


Fig. 3. X-ray diffraction patterns for ZSM-5 and the optimized SZr/Ag, SZr/Ti, SZr/W, and SZr/ZSM-5 calcined 550 °C for 4 h (T = tetragonal, and M = monoclinic phase).

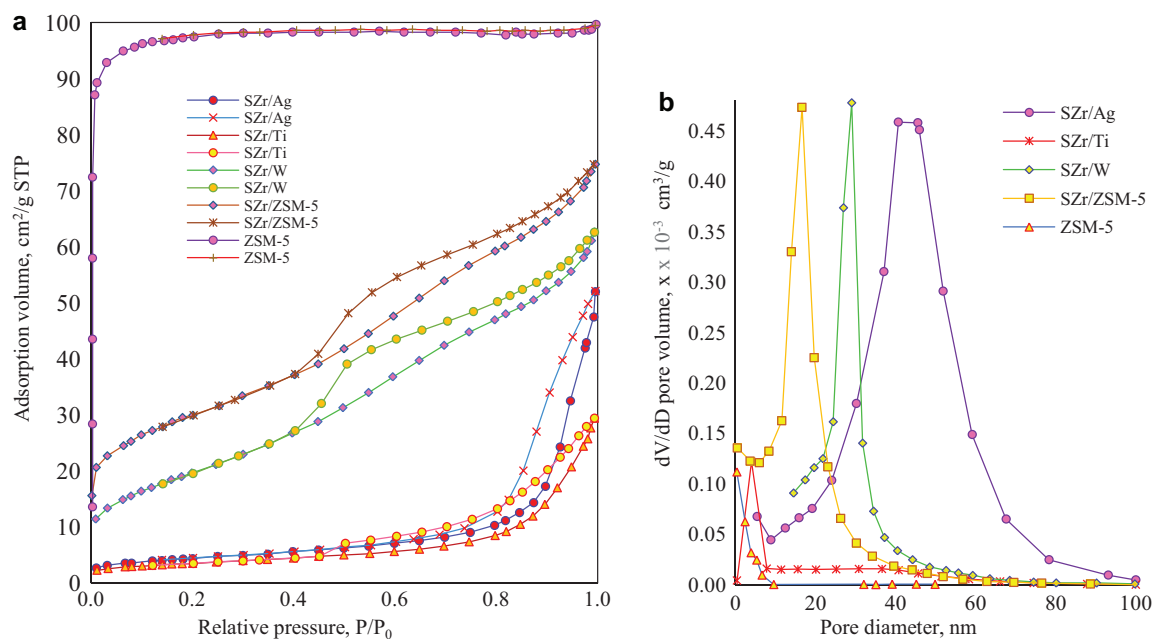


Fig. 4. (a) N₂ adsorption-desorption isotherms for SZr/Ag, SZr/Ti, SZr/W, SZr/ZSM-5, and ZSM-5 respectively, and (b) pore size distribution curves for SZr/Ag, SZr/Ti, SZr/W, SZr/ZSM-5, and ZSM-5 respectively, synthesized under the same conditions.

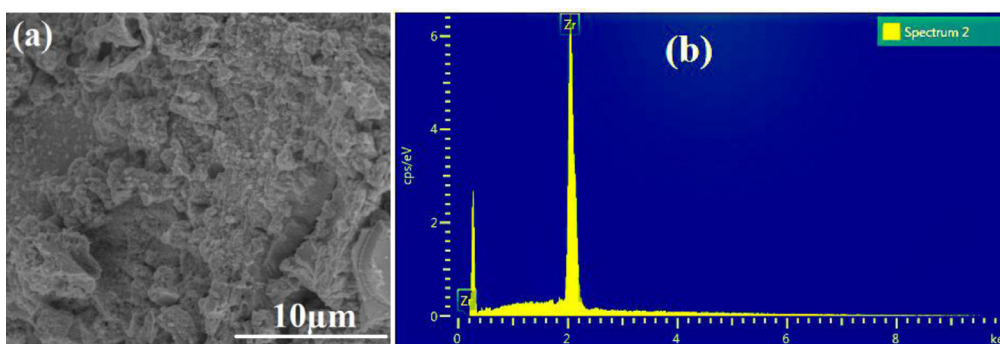


Fig. 5. (a) Results of the surface microstructural analysis of the ZrO_2 via FE-SEM and (b) surface elemental composition of the ZrO_2 determined via EDX analysis.

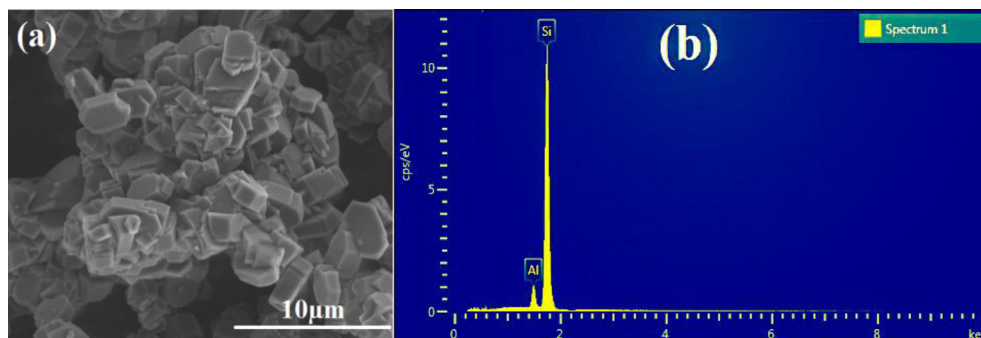


Fig. 6. (a) Results of the surface microstructural analysis of the ZSM-5 via FE-SEM and (b) surface elemental composition of the ZSM-5 determined via EDX analysis.

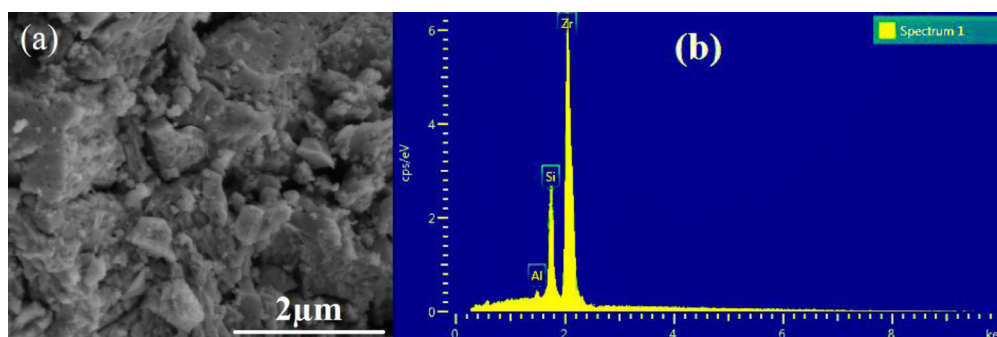


Fig. 7. (a) Results of the surface microstructural analysis of the SZr/ZSM-5 via FE-SEM and (b) surface elemental composition of the SZr/ZSM-5 determined via EDX analysis.

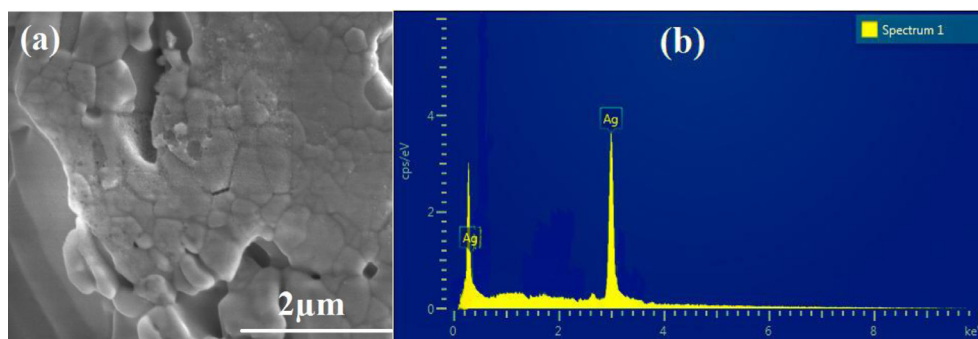


Fig. 8. (a) Results of the surface microstructural analysis of the $AgNO_3$ via FE-SEM and (b) surface elemental composition of the $AgNO_3$ determined via EDX analysis.

(1.26 wt.%). Fissures and faults appeared on the surface of SZr/ZSM-5 which were absent from the parent ZSM-5 and zirconium micrographs. These confirmed secondary pores formation that are beneficial in minimizing diffusion associated with zeolites [42]. Further, agglomeration or the adhesion of particles to each other because of van der Waals forces of attraction is significantly higher in

nanoparticles. Fine particles, particularly nanoscale particles have characteristic large surface areas. These often agglomerate to form either secondary particles or lumps that minimize the interfacial energy or total surface area of the system. Fig. 7(a) evidenced such agglomeration. Similarly, Figs. 8(a) and 9(a) revealed the surface microstructure of $AgNO_3$ and SZr/Ag as studied via FE-SEM. The

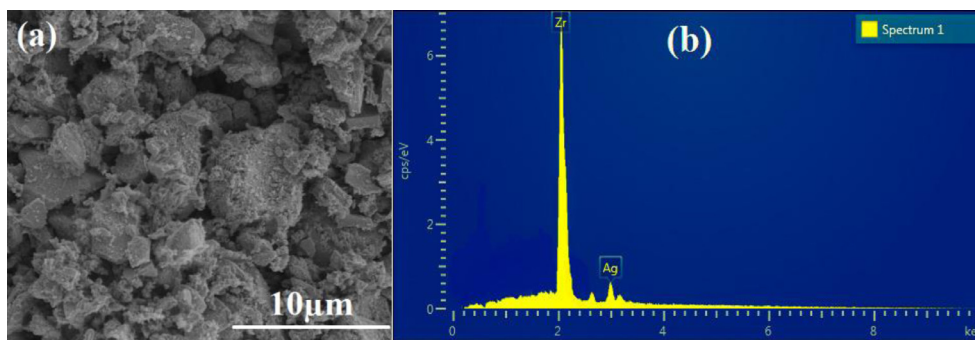


Fig. 9. (a) Results of the surface microstructural analysis of the SZr/Ag via FE-SEM and (b) surface elemental composition of the SZr/Ag determined via EDX analysis.

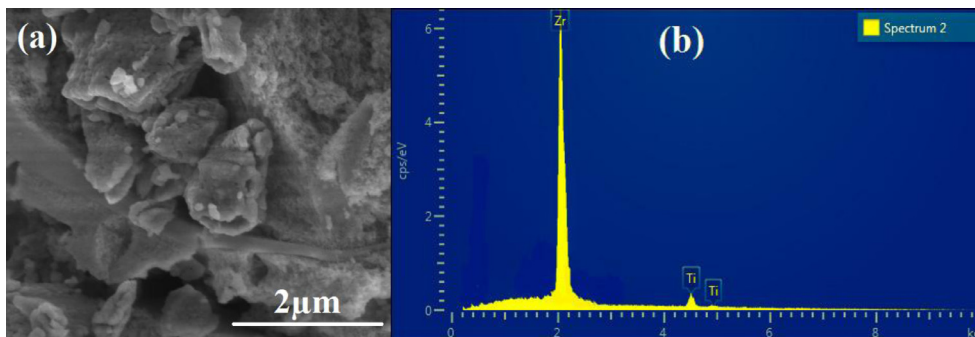


Fig. 10. (a) Results of the surface microstructural analysis of the SZr/Ti via FE-SEM and (b) surface elemental composition of the SZr/Ti determined via EDX analysis.

different constituents were homogeneously processed into solid particles of uniform dimensions. The EDX analysis of the surface elemental composition (Fig. 8b and 9b) revealed the presence of zirconium (99.63 wt.%) and sulfur (0.16 wt.%). Cracks were evident on the surface of the composite catalyst mainly because of its stronger acidity. This clarified the higher mesoporosity and activity of SZr/Ag when compared with that of SZr/Ti and SZr/W.

Similarly, Fig. 9(a) presents the size and shape of topographic features of SZr/Ti catalyst studied via FE-SEM. The surface morphology was also homogeneously processed into solid particles. The surficial elemental composition by EDX analysis (Fig. 9b) also revealed the presence of 92.92 wt.% zirconium, 6.45 wt.% and 0.36 wt.% sulfur.

Figs 11(a) and 12(a) present the surface microstructure of the parent $(\text{NH}_4)_6\text{H}_2\text{W}_{12}\text{O}_{40} \cdot x\text{H}_2\text{O}$ and SZr/W catalyst. High calcination temperature made the zirconium oxide structure to fully agglomerate with the crystal lattices of the tungstate oxide (Fig. 12). This explains the comparative high surface area exhibited by SZr/W. Fig. 12(b) presents a cross-sectional surficial composition and distribution of elements on SZr/W via EDX analysis. Expectedly, a somewhat amorphous phase of the parent material (Fig. 11) transformed into crystalline phase as displayed by the micrograph representing SZr/W as shown in Fig. 12(a).

3.2. Comparative transesterification activity over the composite catalysts

The preferential adsorption of TG and FFA on the Brønsted acid sites of sulfated zirconia facilitates the simultaneous transesterification and esterification reaction and explains the poorer performance exhibited by SZr/W. Hence, the reaction investigated in this study probably follows the Langmuir–Hinshelwood mechanism (Scheme 1) [44]. Brønsted acid protonates the hydroxyl group on the methanol while carbocation results from the protonation of TG and FFA from the adjacent site on catalyst surface. A nucleophile emerges from the deprotonation of methanol oxygen that generates a tetrahedral intermediate from attacking the carbocation. Consequently, the

elimination of water by the tetrahedral intermediate forms ester during esterification. Similarly, it generates a new ester during transesterification by eliminating glycerol. The same mechanism applies for di- and tri-glycerides, which was aided by the highly hydrophobic SZr/ZSM-5. The facile method employed in the present study facilitates good dispersion of the active catalyst component in the pores of the support. This minimizes diffusion limitation such as obstruction of the mouth of pores of the support material.

Morterra et al. [45] posited a linear relationship between increased acidity and the feedstock conversions. To further study the activity of catalysts, simultaneous transesterification of UFO was investigated and presented in Fig. 13. The study revealed an order of conversion ($\text{SZr/ZSM-5} > \text{SZr/Ag} > \text{SZr/Ti} > \text{SZr/W} \gg \text{ZSM-5}$) that showed significant correlation to the acidity and structure of the materials. This further affirms the presence of sulfate active sites within the surface structure of the catalysts as reported by Hino et al. [46]. However, the pore size of SZr/ZSM-5 might have minimized conversion beyond expectation because of possible occlusion. This is because the catalyst possesses 5.10 nm pore size. However, a TG molecule requires a critical diameter or the smallest access cylinder of 2 to 4 nm [41,47]. Srilatha et al. [48] reported severe internal diffusion resistance while López et al. [49] obtained 57% conversion from sulfated zirconia with S_{BET} of $134.4 \pm 5.3 \text{ m}^2/\text{g}$. Premised on the underlying difficulty of the TG molecules to access the inner pores of the catalysts for efficient contact, it is plausible to assert that amount and dispersion of active sites which is reflective of acidity was responsible for transesterification activity reported in this study. It is also instructive to note that infusing sulfate onto zirconium oxide produces acidic solid catalysts. However, doping zirconia with acidic ZSM-5 further increases its acidity. Hence, the high conversions displayed by the synthesized material reflect the role of this incorporation. It is therefore plausible to assert that acidity of materials synthesized in this study have direct correlation to surface hydroxyl groups.

Further, the facile process employed in present study is encouraging considering the lower reaction parameters employed (200 °C, 5 h, 5:1 molar ratio and 2 wt.% catalyst loading). It eliminates the

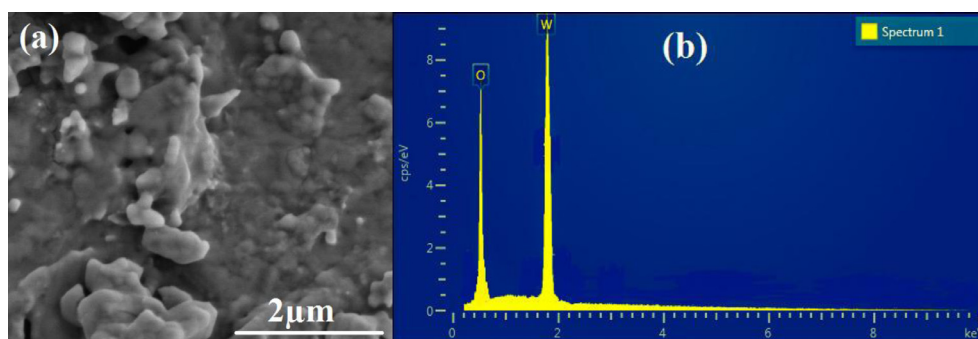


Fig. 11. (a) Results of the surface microstructural analysis of the $(\text{NH}_4)_6\text{H}_2\text{W}_{12}\text{O}_{40} \cdot x\text{H}_2\text{O}$ via FE-SEM and (b) surface elemental composition of the $(\text{NH}_4)_6\text{H}_2\text{W}_{12}\text{O}_{40} \cdot x\text{H}_2\text{O}$ determined via EDX analysis.

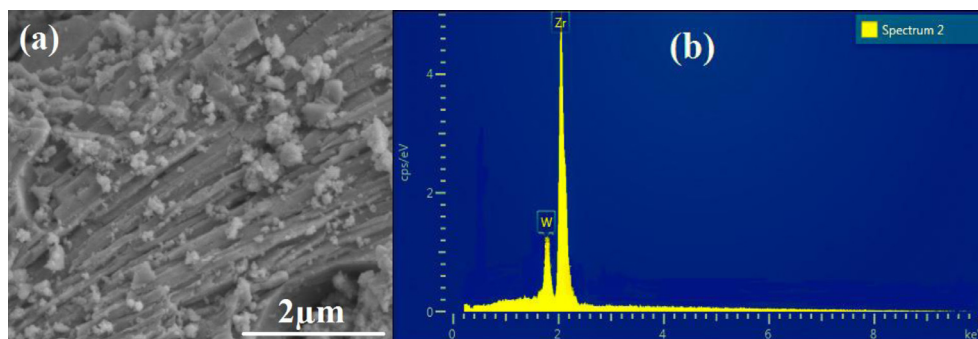
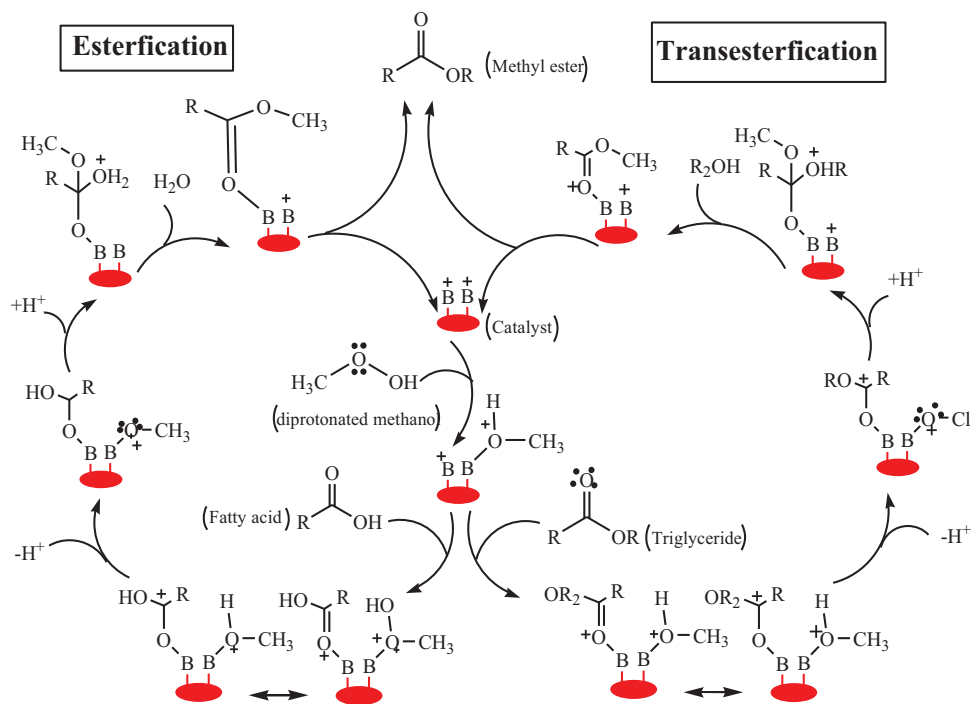


Fig. 12. (a) Results of the surface microstructural analysis of the SZr/W via FE-SEM and (b) surface elemental composition of the SZr/W determined via EDX analysis.



Scheme 1. The Langmuir-Hinshelwood mechanism [adapted from 44].

yield loss and chemical costs associated with acid-catalyzed esterification pretreatment and caustic stripping (Table 3) [50]. This lowers the energy consumption and chemical costs. Against this backdrop, it is important to highlight some related reports for comparison. Danuthai et al. [51] converted *ca.* 100% methyl octanoate over H-ZSM5 at a very high temperature of 500 °C for 5 h. Whereas, Chung and Park [10] obtained 80% conversion from Soybean oil mixed with

oleic acid over H^+ ion exchanged ZSM-5 at 60 °C for 6 h. Moreover, the deactivation limitation associated with sulfated zirconia due to leaching of sulfate ions was not observed from this study. Further, it is worthy to note that conventional zirconia produced negligible conversion under the same conditions. The encouraging conversion of 95% obtained with SZr/Ti from the present study corroborated the findings by López et al. [52]. This is despite the employed calcination

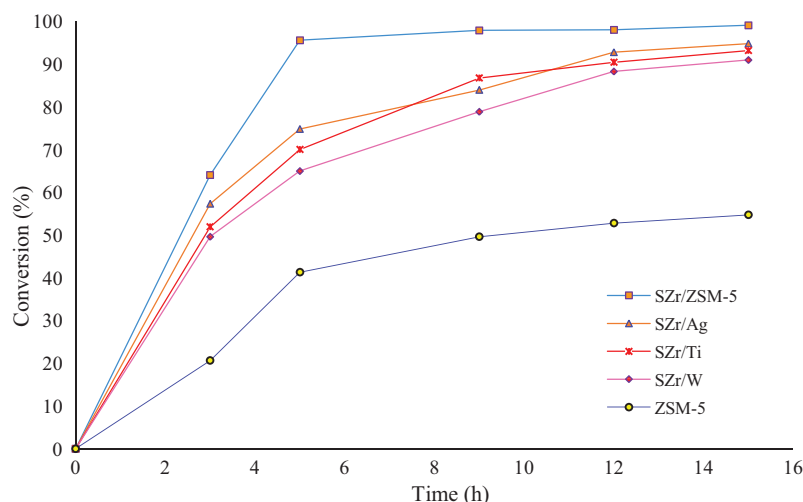


Fig. 13. Catalytic activities of 2 wt.% mesoporous SZr/Ag, SZr/Ti, SZr/W, SZr/ZSM-5, and ZSM-5 catalysts at 5:1 methanol-to-oil ratio and 200 °C.

Table 3

Comparative FFA pretreatment cost [49].

FFA % in oil		2.5%	5%	10%	15%
Caustic stripping	Yield loss	2.5%	5%	10%	15%
	Cost (\$/gal)	0.119	0.238	0.476	0.715
	Cost (\$/L)	0.031	0.063	0.126	0.189
Acid esterification	Yield loss	1%	1%	1%	1%
	Cost (\$/gal)	0.040	0.080	0.160	0.240
	Cost (\$/L)	0.011	0.021	0.042	0.063

Notes: All chemical costs ($H_2SO_4 = \$5/\text{gal}$, methanol = $\$1.6/\text{gal}$, sodium methylate = $\$4/\text{gal}$) and biodiesel selling price ($\$4/\text{gal}$ after various local and federal tax credit and other incentives) were based on recent industrial scale values with 80% assumed efficiency for methanol recovery [49].

temperature of 550 °C. Kiss et al. [12] reported 500 °C, and 400 to 500 °C as optimum calcination temperature for SZr and TiZ respectively, with subsequent loss of activity at higher temperature due to sulfur loss and decreased catalyst's surface area. However, the material showed poor reusability because of active basic sites poisoning from carboxylic acids. This hinders its suitability for transesterification especially with feedstocks containing higher acid values such as UFO. In comparison also, WO_3/ZrO_2 gave ~100% conversion from 4.5:1 methanol-to-soybean oil at 200 °C after 20 h [6]. In a different study similar to the current report, Furuta et al. [6] obtained 70% conversion from UFO over WO_3/ZrO_2 .

Though all the samples exhibited good performances when evaluated for transesterification of UFO after 5 h (Fig. 13), SZr/ZSM-5 exhibited highest activity than the other catalysts. This is despite possessing lower pore size compared to SZr/Ag and SZr/Ti. We attributed this to enhanced acid strength imparted on SZr/ZSM-5 by the zeolite, as well as its suitable S_{BET} when compared to its counterparts. The NH_3 -TPD and IR spectra of pyridine adsorption analyses showed lower acid density for SZr/Ti and SZr/W than that of SZr/ZSM-5. Consequently, the interaction between the zirconia (facilitated by highly dispersed nanoparticles) and higher mesopores of the zeolite support determined the observed acidity and activity. This is because acidity, which arises from electron deficiency of the supported catalysts influences the catalytic properties of the material in two ways. (a) The support effect enhances interaction with the active components. (b) Such interactions provide acidic site that transforms the catalytic material into bifunctional catalyst. Further, we attributed the performance of the other catalysts to a combination of acidity (0.14, 0.09, and 0.05 mmol/g) and the good S_{BET} (20.11, 14.53, and 5.37 nm²) exhibited by SZr/Ag, SZr/Ti, and SZr/W respectively.

4. Conclusions and outlook

This study developed a facile route for synthesizing efficient solid acid catalysts for transesterifying UFO-containing high FFA under moderate reaction conditions. Albeit, doping SZ with ZSM-5 is a key feature of this synthesis strategy that proved superior to prior formulations. This is because despite the destruction of ZSM-5 crystallographic phase, the process stabilized the mesostructure channels, and ensured higher catalytic performance on SZr/ZSM-5. Interestingly, the activity of SZr/ZSM-5 was markedly higher than that of SZr/Ti, SZr/Ag, and SZr/W synthesized under similar conditions. The study provided solutions to the economic concerns associated with accessing fossil fuel reserves *via* simultaneous transesterification and esterification of waste oil into low cost and readily implementable biodiesel as sustainable alternative source of energy for transportation. Furthermore, the use of waste oil is essential in solving the contending issue of regional availability. Other significant findings include: (1) factors essential for efficient transesterification include acidic site, sufficient surface area with mesoporous channels and tetragonal phase of zirconia. (2) The interplay between metal species of modified oxo-anions and pore structure of acidic zeolites and its strong properties enhances acidity of sulfated composite catalysts. (3) The encouraging conversions obtained suggested that activity for transesterification does not depend solely on textural property of the catalytic material. (4) Amount and dispersion of active sites, which are reflective of acidity of the catalysts, play significant role in facilitating higher conversion of TG into biodiesel. (5) The study also showed how to achieve flexibility of properties from unlimited number of possible manipulations from one catalyst precursor. These encouraging observations highlighted the possibility of improving on the reported formulations to facilitate higher intrinsic efficiency in biodiesel production. The catalysts synthesized from the present study have potential applications in other acid-catalyzed reactions such as selective catalytic reactions, SCR for abating environmentally harmful NO_x emissions from mobile or stationary power sources. This is because of the presence of sulfate ions and their resistance to H_2O , which are inevitable components of diesel exhaust gas.

Acknowledgments

The authors are grateful for the support of the research grant from Fundamental Research Grant Scheme (FRGS) with grant no.HIR-MOHE D000038-16001 under University of Malaya, Malaysia and

Tertiary Education Trust Fund (TETFund), Ahmadu Bello University, Zaria, Nigeria.

References

- [1] Hassan SN, Sani YM, Abdul Aziz AR, Sulaiman NMN, Daud WMAW. Biogasoline: an out-of-the-box solution to the food-for-fuel and land-use competitions. *Energy Convers Manage* 2015;89:349–67.
- [2] Sani YM, Alaba AP, Raji-Yahya AO, Abdul Aziz AR, Daud WMAW. Acidity and catalytic performance of Yb-doped $\text{SO}_4^{2-}/\text{Zr}$ synthesized via different preparatory conditions for biodiesel production. *J Taiwan Inst Chem Eng* 2015 <http://dx.doi.org/10.1016/j.jtice.2015.07.016>.
- [3] Guldhe A, Singh B, Rawat I, Bux F. Synthesis of biodiesel from *Scenedesmus* sp. by microwave and ultrasound assisted in situ transesterification using tungstated zirconia as a solid acid catalyst. *Chem Eng Res Des* 2014;92:1503–11.
- [4] Xie W, Wang T. Biodiesel production from soybean oil transesterification using tin oxide-supported WO_3 catalysts. *Fuel Process Technol* 2013;109:150–5.
- [5] Farooq M, Ramli A, Subbarao DJ. Biodiesel production from waste cooking oil using bifunctional heterogeneous solid catalysts. *J Cleaner Prod* 2013;59:131–40.
- [6] Furuta S, Matsuhashi H, Arata K. Biodiesel fuel production with solid superacid catalysis in fixed bed reactor under atmospheric pressure. *Catal Commun* 2004;5:721–3.
- [7] Park YM, Lee DW, Kim DK, Lee JS, Lee KY. The heterogeneous catalyst system for the continuous conversion of free fatty acids in used vegetable oils for the production of biodiesel. *Catal Today* 2008;131:238–43.
- [8] Refaat AA. Biodiesel production using solid metal oxide catalysts. *Int J Environ Sci Technol* 2011;8:203–21.
- [9] Shu Q, Yang B, Yuan H, Qing S, Zhu G. Synthesis of biodiesel from soybean oil and methanol catalyzed by zeolite beta modified with La^{3+} . *Catal Commun* 2007;8:2159–65.
- [10] Chung KH, Park BG. Esterification of oleic acid in soybean oil on zeolite catalysts with different acidity. *J Ind Eng Chem* 2009;15:388–92.
- [11] Danuthai T, Jongpatiwut S, Rirksomboon T, Osuwan S, Resasco DE. Conversion of methyl esters to hydrocarbons over an H-ZSM5 zeolite catalyst. *Appl Catal A* 2009;361:99–105.
- [12] Kiss AK, Omota F, Dimian AC, Rothenberg G. The heterogeneous advantage: biodiesel by catalytic reactive distillation. *Top Catal* 2006;40:141–50.
- [13] Dasari MA, Goff MJ, Suppes GJ. Nonanalytic alcoholysis kinetics of soybean oil. *JAOC* 2003;80:189–92.
- [14] Sasidharan M, Kumar R. Transesterification over various zeolites under liquid-phase conditions. *J Mol Catal A* 2004;210:93–8.
- [15] Breck DW. Zeolite molecular sieves, structure, chemistry and use. New York: J Wiley & Sons; 1974.
- [16] Lotero E, Liu Y, Lopez DE, Suwannakarn K, Bruce DA, Goodwin JG. Synthesis of biodiesel via acid catalysis. *Ind Eng Chem Res* 2005;44:5353–63.
- [17] Narasimharao K, Brown DR, Lee AF, Newman AD, Siril PF, Tavener SJ, et al. Structure–activity relations in Cs-doped heteropolyacid catalysts for biodiesel production. *J Catal* 2007;248:226–34.
- [18] Suwannakarn K, Lotero E, Ngaosuwan K, Goodwin JG. Simultaneous free fatty acid esterification and triglyceride transesterification using a solid acid catalyst with in situ removal of water and unreacted methanol. *Ind Eng Chem Res* 2009;48:2810–18.
- [19] Kouzu M, Nakagaïto A, Hidaka J-S. Pre-esterification of FFA in plant oil transesterified into biodiesel with the help of solid acid catalysis of sulfonated cation-exchange resin. *Appl Catal A* 2011;405:36–44.
- [20] Kaeding WW, Butter SA. Production of chemicals from methanol. *J Catal* 1980;61:155–64.
- [21] Rezaei M, Alavi SM, Sahebdelfar S, Bai P, Liu XM, Yan ZF. CO_2 reforming of CH_4 over nanocrystalline zirconia-supported nickel catalysts. *Appl Catal B* 2008;77:346–54.
- [22] Rezaei M, Alavi SM, Sahebdelfar S, Qian L, Yan Z-F. CO_2 - CH_4 reforming over nickel catalysts supported on mesoporous nanocrystalline zirconia with high surface area. *Energy Fuels* 2007;21:581–9.
- [23] Guan B, Wang T, Zeng S, Wang X, An D, Wang D, et al. A versatile cooperative template-directed coating method to synthesize hollow and yolk-shell mesoporous zirconium titanium oxide nanospheres as catalytic reactors. *Nano Res* 2013;7:246–62.
- [24] Zou H, Lin YS. Structural and surface chemical properties of Sol-Gel derived TiO_2 - ZrO_2 oxides. *Appl Catal A* 2004;265:35–42.
- [25] Čejka J, Richter M, Kölsch P. Characterization of external surface properties of zeolite ZSM-5 modified by 12-tungstosilicic acid. In: Beyer HK, Nagy JB, Karge HG, Kiricsi I, editors. *Studies in surface science and catalysis*, vol. 94. Amsterdam, New York: Elsevier; 1995. p. 246–53.
- [26] Song C, Lai WC, Schmitz AD, Reddy KM. Characterization of acidic properties of microporous and mesoporous zeolite catalysts using TGA and DSC (No. CONF-960376–, TRN: 96:003805-0353). Washington, DC (United States): American Chemical Society; 1996.
- [27] Das D, Mishra HK, Dalai AK, Parida KM. Isopropylation of benzene over sulfated ZrO_2 - TiO_2 mixed-oxide catalyst. *Appl Catal A* 2003;243:271–84.
- [28] Mile B, Stirling D, Zammitt MA, Lovell A, Webb M. TPR studies of the effects of preparation conditions on supported nickel catalysts. *J Mol Catal* 1990;62:179–98.
- [29] Manriquez ME, López T, Gómez R, Navarrete J. Preparation of TiO_2 - ZrO_2 mixed oxides with controlled acid-basic properties. *J Mol Catal A* 2004;220:229–37.
- [30] Jacobs PA, Von Ballmoos R. Framework hydroxyl groups of H-ZSM-5 zeolites. *J Phys Chem* 1982;86:3050–2.
- [31] Ward JW. The nature of active sites on zeolites: X. The acidity and catalytic activity of X zeolites. *J Catal* 1969;14:365–78.
- [32] Angell CL, Schaffer PC. Infrared spectroscopic investigations of zeolites and adsorbed molecules. I. Structural OH groups. *J Phys Chem* 1965;69:3463–70.
- [33] Parry EP. Catalytic properties of sulfated and non-sulfated ZrO_2 - SiO_2 . *J Catal* 1963;2:371–9.
- [34] Jin F, Li Y. A FTIR and TPD examination of the distributive properties of acid sites on ZSM-5 zeolite with pyridine as a probe molecule. *Catal Today* 2009;145:101–7.
- [35] Emeis CA. Determination of integrated molar extinction coefficients for infrared absorption bands of pyridine adsorbed on solid acid catalysts. *J Catal* 1993;141:347–54.
- [36] Lu R, Tangbo H, Wang Q, Xiang S. Properties and characterization of modified HZSM-5 zeolites. *J Nat Gas Chem* 2003;12:56–62.
- [37] Suzuki K, Sastre G, Katada N, Niwa M. Quantitative Measurements of Brønsted acidity of zeolites by ammonia IRMS-TPD method and density functional calculation. *Chem Lett* 2007;36:1034–5.
- [38] Pan F, Lu X, Zhu Q, Zhang Z, Yan Y, Wang T, et al. A fast route for synthesizing nano-sized ZSM-5 aggregates. *J Mater Chem A* 2014;2:20667–75.
- [39] Santos V, Zeni M, Bergmann CP, Hohemberger JM. Correlation between thermal treatment and tetragonal/monoclinic nanostructured zirconia powder obtained by sol-gel process. *Rev Adv Mater Sci* 2008;17:62–70.
- [40] Osendi MI, Moya JS, Serna CJ, Soria J. Metastability of tetragonal zirconia powders. *J Am Ceram Soc* 1985;68:135–9.
- [41] Fernandez MB, Tonetto GM, Crapiste G, Damiani DE. Kinetics of the hydrogenation of sunflower oil over alumina supported palladium catalyst. *Int J Chem Reactor Eng* 2007;5:10.
- [42] Sing KSW, Everett DH, Haul RAW, Moscou L, Pierotti RA, Rouquerol J, et al. Reporting physisorption data for gas/solid systems with special reference to the determination of surface area and porosity. *Pure Appl Chem* 1985;57:603–19.
- [43] Sato K, Nishimura Y, Shimada H. Preparation and activity evaluation of Y zeolites with or without mesoporosity. *Cata Lett* 1999;60:83–7.
- [44] Dussadee R, Adam H, Penjit S. Simultaneous conversion of triglyceride/free fatty acid mixtures into biodiesel using sulfated zirconia. *Top Catal* 2010;53:773–82.
- [45] Morterra C, Cerrato G, Pinna F, Signoreto M. Crystal phase, spectral features, and catalytic activity of sulfate-doped zirconia systems. *J Catal* 1995;157:109–23.
- [46] Hino M, Kurashige M, Matsuhashi H, Arata K. The surface structure of sulfated zirconia: studies of XPS and thermal analysis. *Thermochimica* 2006;441:35.
- [47] Kiss AA, Dimian AC, Rothenberg G. Solid acid catalysts for biodiesel production—towards sustainable energy. *Adv Synth Catal* 2006;348:75–81.
- [48] Srilatha K, Kumar C, Prabhavathi Devi BLA, Prasad RBN, Sai Prasad PS, Lingaiah N. Efficient solid acid catalysts for esterification of free fatty acids with methanol for the production of biodiesel. *Catal Sci Technol* 2011;1:662–8.
- [49] López DE, Goodwin JG Jr, Bruce DA, Lotero E. Transesterification of triacetin with methanol on solid acid and base catalysts. *Appl Catal A* 2005;295:97–105.
- [50] Chai M, Tu Q, Lu M, Yang YJ. Esterification pretreatment of free fatty acid in biodiesel production from laboratory to industry. *Fuel Proc Technol* 2014;125:106–13.
- [51] Danuthai T, Jongpatiwut S, Rirksomboon T, Osuwan S, Resasco DE. Conversion of methyl esters to hydrocarbons over an H-ZSM5 zeolite catalyst. *Appl Catal A* 2009;361:99–105.
- [52] López DE, Goodwin JG Jr, Bruce DA, Furuta S. Esterification and transesterification using modified-zirconia catalysts. *Appl Catal A* 2008;339:76–83.